Mining, Metallurgy & Exploration (2024) 41:277–286
https://doi.org/10.1007/s42461-023-00902-2

Study on the Guiding Mechanism of Multiple and Empty Holes Under Explosion Load

Ruyang Cao[1] · Yunpeng Li[1] · Chun Feng[2,3] · Yiming Zhang[1]

Received: 27 July 2023 / Accepted: 12 December 2023 / Published online: 19 December 2023

Abstract
In the past, the selection of the number of empty holes between blast holes heavily relied on the subjective experience of practitioners, leading to unsatisfactory blasting results. The number of empty holes between blast holes is particularly important for the perforation of explosive cracks. In order to determine the optimum number of empty holes for inducing the propagation of explosive cracks, a two-dimensional numerical model of two-hole blasting was established based on the continuous-discontinuous element method (CDEM) using polymethyl methacrylate (PMMA) as the medium, and numerical simulation of various working conditions was conducted; the simulation results are basically consistent with the PMMA model test. Through the analysis of blasting parameters, the optimal number of empty holes with a certain hole spacing is fitted. The following conclusions are drawn: (1) There is a threshold for variable x. When x exceeds 50, the presence of empty holes cannot lead to the perforation of explosive cracks between the blast holes. (2) When x is below 50, the optimal number of empty holes inducing the propagation of explosive cracks can be determined through fitting an empirical formula. By adjusting the number of empty holes between blast holes, a significant spacing between adjacent blast holes was achieved, allowing for effective penetration, so as to effectively "induce" the direction of the fracture zone and make full use of the energy of explosives. The research results of this paper are conducive to the research of directional blasting technology and provide certain references for the optimization of precision blasting parameters.

Keywords Induced hole · CDEM · Crack propagation · Double hole blasting · Precise blasting

1 Introduction

Blasting technology is characterized by its simple process and strong adaptability to engineering geology, making it widely used in various fields such as tunnel excavation, road cuttings, mining operations, and water resources and hydropower projects, resulting in significant social and economic benefits [1–3]. Since the last century, numerous scholars have conducted experimental and theoretical research on rock blasting processes and reached the conclusion that the combined effect of stress waves and gas pressure is a common cause of rock fracture and fragmentation [4–6].

Based on the aforementioned mechanism of rock blasting, numerous scholars have explored the behavior of crack propagation and penetration in blast-induced fracturing. Zhao [7] investigated the fracture patterns of coal during the blasting process using the LS-DYNA software, and concluded that the initiation and propagation of cracks between adjacent boreholes are closely related to the delay time of detonation. Hu [8] established deformation control equations and successfully described the deformation and damage process of gas-containing coal through numerical calculations, thereby addressing the fluid–solid coupling problem in gas and coal engineering practices. Guo [9] conducted numerical simulations on the propagation laws of dual-hole blast-induced cracks based on the superposition effect of stress waves, and concluded that the superposition effect of stress waves promotes the penetration of cracks. Yang [10, 11] conducted model experiments to study the dynamic behavior

✉ Yunpeng Li
202311601008@stu.hebut.edu.cn

[1] School of Civil and Transportation Engineering, Hebei University of Technology, Xiping Road 5340, Tianjin 300401, China

[2] Institute of Mechanics, Chinese Academy of Sciences, North 4th Ring West Road 15, Beijing 100190, China

[3] School of Engineering Sciences, University of Chinese Academy of Sciences, Yuquan Road 19, Beijing 100049, China

of crack penetration between two boreholes under dual-hole blasting and different slotting methods. They obtained the propagation patterns of dual-hole blast-induced cracks and investigated the variation of stress intensity factors at the crack tips, qualitatively analyzing the interaction mechanism between the explosive stress wave and the crack tip. The above-mentioned studies have explored the penetration laws of dual-hole blast-induced cracks through numerical simulations or experiments, providing a certain understanding of their mechanisms.

Empty holes provide excellent guidance for blast-induced main cracks. Currently, in engineering projects such as tunnel excavation and roadway construction, the use of central empty holes during blasting has proven to be highly effective, significantly increasing the speed of excavation. Many scholars have conducted extensive research on the propagation behavior of blast-induced cracks in the presence of defects and empty holes. Nakamura [12] conducted experiments on controlling crack propagation and analyzed the influence of regular empty holes and notches on both sides of the empty hole on crack propagation. Cho [13] combined numerical simulations with experiments to study the directional fracture effect of empty holes. Yang [14] used digital laser dynamic speckle method to investigate the crack propagation behavior of polymethyl methacrylate materials with pre-existing cracks under the action of explosive stress waves, providing valuable experimental evidence for evaluating and designing controlled blasting in rock excavation. Dally [15] employed dynamic photoelasticity to study the propagation process of explosive stress waves and their interaction with cracks and cavities.

However, in blasting construction, it is challenging to select the spacing between blast holes and the number of empty holes, leading to adverse blasting phenomena such as excessive fragmentation. Choosing an appropriate number of empty holes can improve blasting efficiency and save explosive consumption. The aforementioned research work provides strong theoretical guidance for the application of empty holes in rock blasting engineering. However, it has limitations as it only explores the penetration laws of blast-induced cracks between blast holes without any empty hole or with a single empty hole. Due to cost and scale limitations, it is challenging to conduct large-scale experimental investigations on dual-hole blasting, resulting in limited understanding of the dynamic behavior of blast-induced cracks influenced by multiple empty holes between blastholes. The work and innovations presented in this paper are as follows:

1. This paper establishes a numerical model for dual-hole blasting using the continuous-discontinuous element method (CDEM) for numerical simulations to analyze the crack propagation and compare it with experimental results, thereby validating the correctness of the two-dimensional numerical model.
2. By varying the number of empty holes, this study investigates their influence on the behavior of blast-induced crack propagation and identifies the optimal number of empty holes that induce crack penetration. Empirical formulas are derived by fitting the simulated data.

The research findings in this paper provide valuable references for the precise selection of the number of empty holes in blasting operations.

2 Numerical Methods and Mechanical Models

2.1 Numerical Methods

The continuous-discontinuous element method (CDEM) is currently widely used in the field of geotechnical engineering dynamics; it is an explicit dynamic numerical method that couples the finite element method with the discrete element method [16–20]. The CDEM is based on the establishment of control equations using the Lagrangian energy system [21–24]. The equation is shown as

$$\frac{\mathrm{d}}{\mathrm{d}t}\left(\frac{\partial L}{\partial v_i}\right)+\frac{\partial L}{\partial u_i}=Q_i \tag{1}$$

where v_i and u_i are generalized coordinates; L is energy of Lagrangian system; Q_i is work done by non-conservative forces. Subsequently, dynamic relaxation method was used to solve the problem, which avoided the need for solving the overall stiffness matrix in traditional finite element methods and improved computational efficiency.

The numerical model in CDEM consists of two parts: the block elements and the interface. The block elements represent the continuous characteristics of the material, such as plasticity, elasticity, and damage. The interface, which exists along the common boundaries between two block elements, represents the discontinuous features of the material, such as fracture, slip, and collision. The interface includes two concepts: the real interface and the virtual interface. Figure 1 illustrates a schematic diagram of the numerical model in CDEM, where Fig. 2c depicts the real interface as solid lines and the virtual interface as dashed lines. The real interface is used to represent the boundaries of each block element. At the same time, the virtual interface exists between two block elements; it connects two block elements using normal springs and tangential springs. When the limit is reached, the springs fracture, resulting in tensile and shear failures.

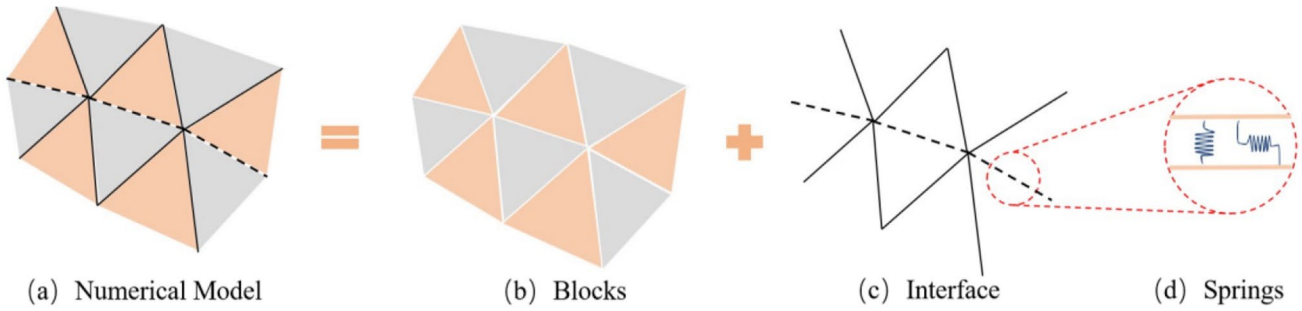

Fig. 1 Composition of numerical model in CDEM

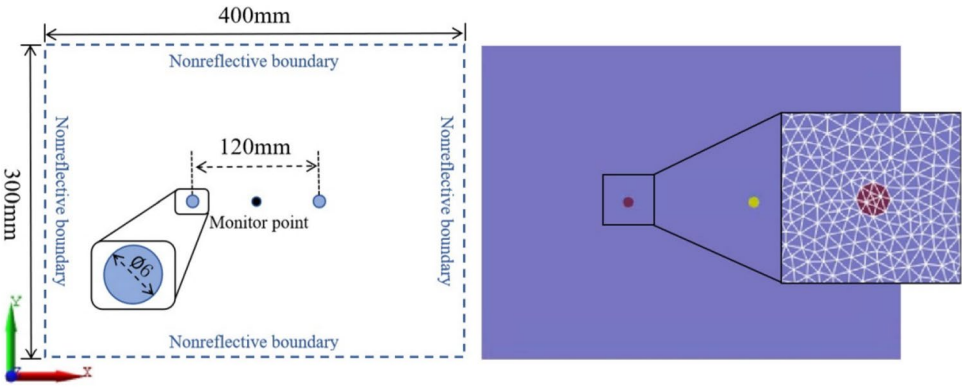

Fig. 2 Numerical model and numerical grid

2.2 Mechanical Models

In this study, the elements are modeled using a linear elastic constitutive model [25]. The equation is shown as

$$\left.\begin{aligned}\Delta\sigma_{ij} &= 2G\Delta\varepsilon_{ij} + \left(K - \frac{2}{3}G\right)\Delta\theta\delta_{ij} \\ \sigma_{ij}(t_1) &= \Delta\sigma_{ij} + \sigma_{ij}(t_0)\end{aligned}\right\} \tag{2}$$

where σ_{ij} is stress tensor; $\Delta\sigma_{ij}$ is increment of stress tensor; $\Delta\varepsilon_{ij}$ is increment of strain tensor; $\Delta\theta$ is increment of volumetric strain; K is bulk modulus; G is shear modulus; δ_{ij} is Kronecker delta symbol; t_0 and t_1 are current time step and next time step.

The virtual interface utilizes a combined tension-shear constitutive model to calculate damage and fracture. The assessment of tensile and shear fractures takes into account the tensile fracture energy and shear fracture energy. Firstly, an incremental approach is employed to calculate the normal and tangential connecting forces on the springs of the virtual interface for the next time step. Then, the following criterion is used to determine tensile fracture.

If

$$-F_n(t_1) \geq \sigma_t(t_0)A_c$$

Then

$$\left.\begin{aligned}F_n(t_1) &= -\sigma_t(t_0)A_c \\ \sigma_t(t_1) &= -\frac{{\sigma_{t_0}}^2\Delta u_n}{2G_{\mathrm{ft}}} + \sigma_{t_0}\end{aligned}\right\} \tag{3}$$

where F_n is normal contact force on the spring; σ_{t_0}, $\sigma_t(t_0)$, and $\sigma_t(t_1)$ are tensile strengths of the virtual interface at the initial time, current time, and next time; A_c is area of the virtual interface; Δu_n is normal relative displacement on the virtual interface at the current time; G_{ft} is tensile fracture energy.

The following criterion is used to determine shear fracture.

If

$$F_s(t_1) \geq F_n(t_1)tan\ \phi + c(t_0)A_c$$

Then

$$\left.\begin{aligned}F_s(t_1) &= F_n(t_1)tan\ \phi + c(t_0)A_c \\ c(t_1) &= -\frac{{c_0}^2\Delta u_s}{2G_{\mathrm{fs}}} + c_0\end{aligned}\right\} \tag{4}$$

where F_s is tangential contact force on the spring; ϕ is internal friction angle of the virtual interface; c_0, $c(t_0)$, and $c(t_1)$ are cohesive forces of the virtual interface at the initial time, current time, and next time; Δu_s is tangential relative displacement on the virtual interface at the current time; G_{fs} is shear fracture energy.

The Lando-Stanyukovich detonation model [26] was adopted to simulate the explosion of the explosives; the model is mainly based on the Lando-Stanyukovich formula, which is shown as

$$\left.\begin{array}{l} PV^{\gamma} = P_0 {V_0}^{\gamma}, P \geq P_k \\ PV^{\gamma_1} = P_k {V_k}^{\gamma_1}, P < P_k \end{array}\right\} \tag{5}$$

where γ =3; γ_1=4/3; P is transient pressure of high-pressure balloon; V is volume of high-pressure balloon; P_0 is initial pressure of high-pressure balloon; V_0 is volume of the explosive charge; P_k and V_k are pressure and volume of high-pressure balloon at boundaries of two adiabatic processes. The expression of P_k is shown as

$$P_k = P_0 \left\{ \frac{\gamma_1 - 1}{\gamma - \gamma_1} \left[\frac{(\gamma - 1) Q_{\omega} \rho_{\omega}}{P_0} - 1 \right] \right\}^{\frac{\gamma}{\gamma - 1}} \tag{6}$$

where Q_{ω} is explosive heat, J/kg; ρ_{ω} is charge density, kg/m^3. The expression of P_0 is shown as

$$P_0 = \frac{\rho_{\omega} D^2}{2(\gamma + 1)} \tag{7}$$

where D is detonation velocity, m/s.

When the program is implemented, the explosion pressure of the element is first calculated according to formula (5), and then, the pressure is converted into the node force of the unit, and the node force contributed by each explosive unit is accumulated to form the joint force. The acceleration, velocity, and displacement of the node are calculated according to Newton's law, and the current volume of the unit is calculated according to the node displacement. The explosion pressure of the next step is calculated according to the current volume and Eq. (5). In this study, the surrounding rock element and the explosive element share nodes, and the explosive pressure generated by the explosive element automatically act on the surrounding rock mass through the common node.

3 Numerical Simulation

3.1 Numerical Model

Using Gmsh for numerical modeling, a two-dimensional planar model was constructed as shown in Fig. 2. The numerical model was divided into 20,536 triangular elements with a grid size of 5 mm. The model has a length of 0.4 m and a height of 0.3 m. In order to investigate the stress variation between blast holes, a monitor point was selected on the cross-section between the two blast holes, as shown in Fig. 2. The monitor point is located at the midpoint of the line connecting the two blast holes. The model material is polymethyl methacrylate (PMMA), which has mechanical properties very similar to rocks. It is a typical quasi-brittle material widely used in the field of explosive impact [27, 28].

Table 1 Model mechanical parameters

Material properties	Units	Value
Density ρ	(kg/m^3)	1187
Elastic modulus E	(GPa)	6.1
Poisson's ratio v	(-)	0.31
Cohesion force c	(MPa)	25
Tensile strength f_t	(MPa)	25
Normal stiffness of springs K_n	(GPa)	5×10^5
Tangential stiffness of springs K_s	(GPa)	5×10^5
Cohesion force c_1	(MPa)	50
Internal friction angle f	(°)	35
Tensile strength f_{t1}	(MPa)	10
tensile fracture energy G_{ft}	(Pa • m)	10
shear fracture energy G_{fs}	(Pa • m)	10

Table 2 Parameters of explosives

Material properties	Units	Value
Charge density ρ_w	(kg/m^3)	1630
Detonation velocity D	(m/s)	4478
Explosion heat Q_w	(J/kg)	3.1×10^6
Initial adiabatic index γ	(-)	3
Adiabatic index at second stage γ_1	(-)	1.333

The input parameters of the model mainly include the block density, elastic modulus, Poisson's ratio, cohesion force, and tensile strength for the calculation of the plastic deformation of the element, and the normal stiffness of springs, tangential stiffness of springs, cohesion force, internal friction angle, tensile strength, shear fracture energy, and tensile fracture energy are used to calculate the damage fracture of the virtual interface; the main mechanical properties of PMMA are shown in Table 1. Explosive parameters are mainly input charge density, explosive speed and explosive heat, and other parameters; the explosive used is lead azide, and its main parameters are shown in Table 2 [29].

3.2 Numerical Model Validation

We simulated the blasting test of a double-hole polymethyl methacrylate (PMMA) specimen and obtained the crack propagation patterns under double-hole blasting as shown in Fig. 3. As shown in Fig. 3a, the two blast holes are at the same horizontal level, while in Fig. 3b, the two blast holes are not at the same horizontal level, with a vertical height difference of 30 mm. Both conditions have a blast

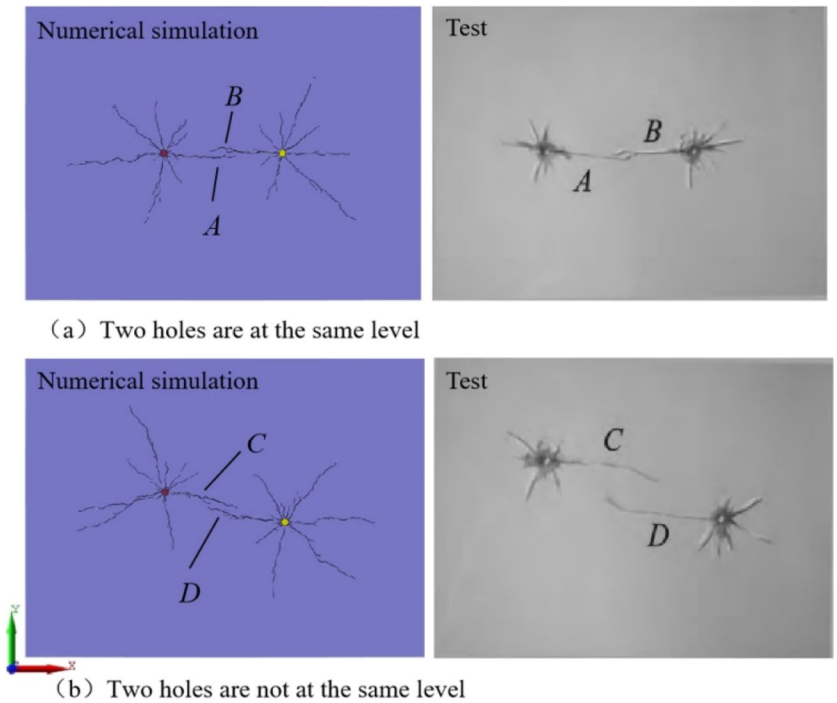

Fig. 3 Comparison between numerical simulation and experimental results

hole diameter of $R = 6$ mm and a blast hole spacing of $L = 120$ mm. From the figures, it can be observed that the crack propagation patterns are similar for both conditions. Radial cracks are observed at the blast hole locations, and the cracks between the blast holes are approximately horizontal and develop towards each other. The cracks *A*, *B*, and *C*, *D* exhibit an approximately rotational symmetry about the midpoint of the two blast holes. In the experiment, the PMMA material in the blast hole wall area was pulverized due to the impact wave. However, in the current numerical simulation, the fragmentation zone cannot be accurately represented and is primarily accounted for by the crack propagation. Therefore, the crack lengths in the numerical simulation are longer compared to the experimental results. However, the number and direction of the main cracks are consistent with the experiment, and the radial crack distribution at the blast hole locations is in good agreement with the experiment.

In addition, the displacement angles of the main cracks A and C during their development between the blast holes were statistically analyzed, and the results were plotted in a curve graph as shown in Fig. 4. From the graph, it can be observed that the displacement angles of the cracks change continuously as the main cracks propagate and develop. In the initial stage of crack development, the change in angle is relatively small, ranging mostly within 0–7°. However, when the crack length exceeds 42 mm, the cracks experience significant deviation angles. This is mainly due to the crack propagation towards weaker areas under the explosive load. The main crack region between the blast holes is weaker

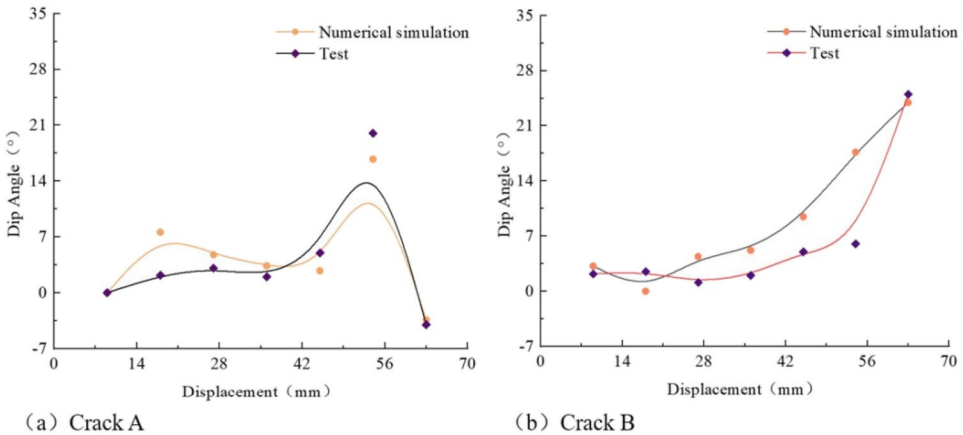

Fig. 4 Comparison between numerical simulation and experimental results

compared to the surrounding intact PMMA material. When the main crack length exceeds 42 mm, the tips of the two cracks gradually approach each other, exhibiting a trend of interconnected development. They "induce" each other, resulting in significant angular deviation at the crack tips. This characteristic is highly consistent with the experimental results.

3.3 Evolutionary Patterns of Damage in Double-Hole Blasting

In addition, due to the extremely short duration of the explosion process, it is challenging to capture the damage of PMMA during the explosion experiment. Focusing on the condition where the two blast holes are at the same horizontal level, a vertical maximum principal stress contour map was generated as shown in Fig. 5. The monitor point in the figure is located at the midpoint of the line connecting the two blast holes.

At $T=0$ μs, both blast holes are simultaneously detonated, resulting in a strong explosive shock wave impacting the blast hole walls and subjecting them to high compressive stresses. At $T=22$ μs, the explosive shock wave transitions into a stress wave and rapidly propagates outward in a concentric circular pattern. At this stage, the instantaneous dynamic pressure of the explosive stress wave exceeds the dynamic compressive strength of the surrounding medium, causing the PMMA in the blast hole region to be compressed and develop microcracks. At $T=32$ μs, the explosive stress waves from the two blast holes meet and superimpose, resulting in peak compressive stress values that still exceed the dynamic compressive strength of PMMA. This leads to the opening and further development of microcracks, eventually forming the main cracks *A* and *B*; simultaneously, the crack tip produces stress concentration effect. Under the effect of the explosive stress waves, the main cracks *A* and *B* exhibit a tendency to develop towards each other. At $T=63$ μs, the explosive stress waves continue to propagate outward. With the superposition of stress waves, the stress near the observation point changes from compressive stress to tensile stress. The main cracks *A* and *B* experience rapid development, taking on an approximately horizontal orientation along the line connecting the two blast holes, but without complete connection. At $T=82$ μs, the stress near the observation point remains tensile. The main cracks *A* and *B* continue to develop towards each other, exhibiting a tendency to interconnect. However, the development rate is slightly reduced compared to the previous moment. At the end of the calculation, the developed crack patterns are shown in the left image of Fig. 3a. The cracks have propagated more extensively, deviating due to the crack growth towards weaker areas under the explosive load. The main cracks *A* and *B* show significant angular deviation.

4 Central Hole Effect

An additional circular hole with a diameter of 6 mm was introduced between the two blast holes for numerical simulation. The hole was positioned at the center of the numerical model, with a blast hole spacing of $L=156$ mm. The simulation results are shown in the top left corner of Fig. 6. Furthermore, to observe the damage process of PMMA, the

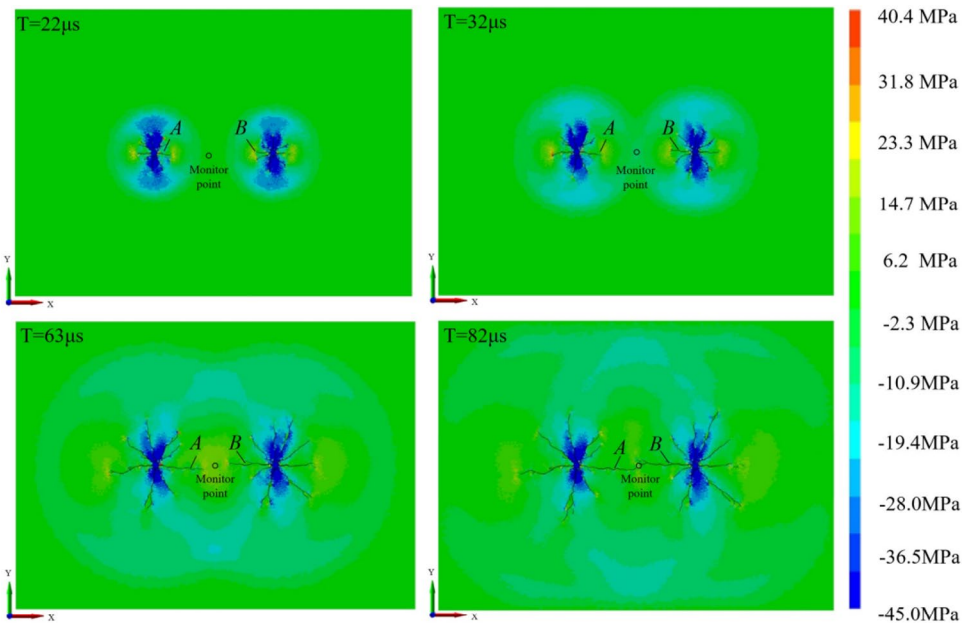

Fig. 5 Contours of stress wave and blasting damage evolution

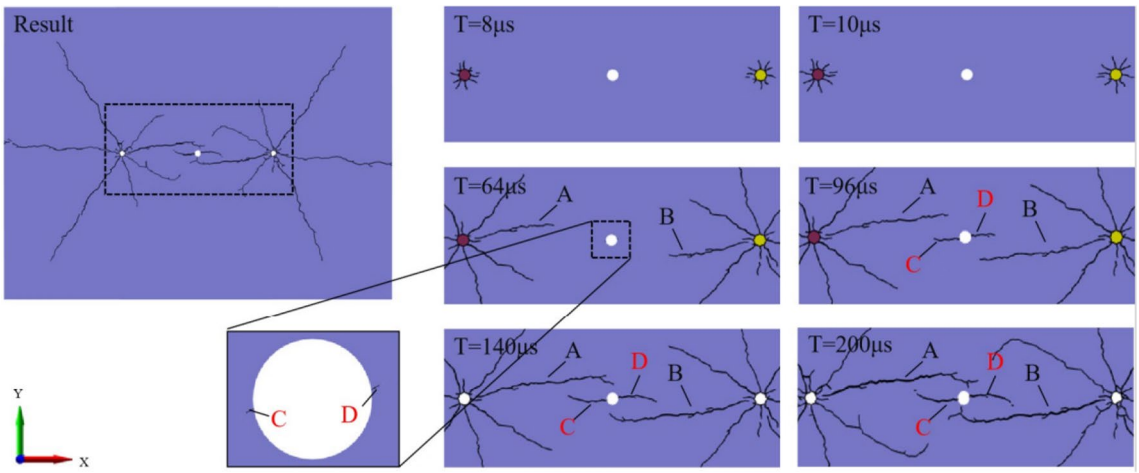

Fig. 6 Contours of fracture evolution in double-hole blasting with empty hole

evolution of cracks in the presence of the void was depicted in the right side of Fig. 6.

From the initiation of the explosive to 8 μs, under the impact of the explosive shock wave, the PMMA in the blast hole wall region experienced intense compressive stress exceeding its compressive strength, resulting in the formation of microcracks. Subsequently, the crack tip produces stress concentration effect and driving the cracks to further propagate. At $T = 10$ μs, the cracks had developed further, as shown in the figure. At $T = 64$ μs, the main cracks *A* and *B* experienced rapid development under the effect of the explosive stress wave. At this stage, wing cracks *C* and *D* appeared on the void-facing side, resulting from the free surface effect of the void and stress concentration, causing tensile stress that exceeded the tensile strength of PMMA and resulted in cracking. At T = 96 μs, the main cracks *A* and *B* continued to develop under the effect of the explosive stress wave. Meanwhile, wing cracks *C* and *D* extended horizontally towards the two blast holes, showing an overlapping effect with the main cracks *A* and *B*. At $T = 140$ μs, the explosive event had ended. Main cracks *A*, *B*, and wing cracks *C*, *D* underwent redirection. Due to the lack of rock mass constraint on the free surface of the void, the main cracks *A* and *B* developed towards the void. Additionally, due to crack growth towards weaker areas under the explosive load, the wing cracks underwent redirection towards cracks *A* and *B*. After 140 μs, the explosion energy has not completely dissipated, and the cracks in the wall of the blasting hole have further expanded. The calculation concluded at $T = 200$ μs, by which time the cracks had developed more extensively compared to 140 μs.

The presence of empty holes has an inducing effect on the initiation of explosive-generated fractures; in this study, we investigate the inducing effect of multiple empty holes between blast holes on the behavior of interconnected fractures during blasting. Averaged along the line connecting the blast holes, n ($n = 0, 1, 2\ldots$) empty holes with a diameter of R, which is the same as the blast hole diameter, are arranged as shown in Fig. 7.

The letter l represents the spacing between empty holes, while the letter L represents the spacing between blast holes. Additionally, the letter L_1 is defined as the effective penetration distance, and the formula for calculating it is as follows:

$$L_1 = L - nR \tag{8}$$

The effective penetration efficiency, denoted as f, can be calculated using the following formula:

$$f = L_1/L \tag{9}$$

Due to model size limitations, the length of the two-dimensional numerical model has been increased from 0.4 to 0.6 m. Three different working conditions are considered: condition 1: Charge mass of 2.830 mg in blast holes; condition 2: charge mass of 5.024 mg in blast holes; condition 3: charge mass of 7.850 mg in blast holes. At the same time, the diameter of the gun hole is 3 mm, 4 mm, and 5 mm, respectively in the three working conditions, and the loading quality of the gun hole is adjusted by adjusting the diameter of the gun hole. At the same time, the diameter of the empty holes between the holes is the same as that of the holes.

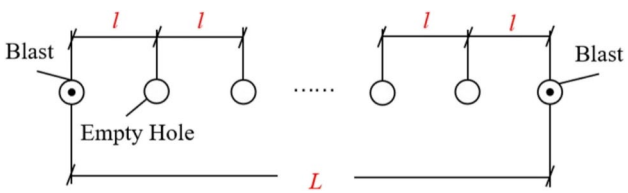

Fig. 7 Schematic of empty hole arrangement

Numerical simulations were conducted for different hole spacing values L under the three given working conditions to deduce the minimum value of coefficient n at which crack perforation occurs due to explosive action. The symbol x is defined as the blasting coefficient, and its calculation formula is as follows:

$$x = \frac{\mathrm{L}}{2}\sqrt{\frac{\pi\rho_{\omega}h}{M}} \tag{10}$$

where L is spacing between holes, m; ρ_{ω} is the charge density, kg/m^3; M is charge mass, kg; h is charge depth, m, which is set to 0.001 m in this study.

The simulation results are presented in Table 3, and the relationships between L and n, as well as f, are plotted in Fig. 8a and b, respectively. From the observations in Table 3, it can be seen that in condition 1, when $L=0.36$ m, cracks with $n=8$–11 cannot be induced to propagate completely. Similarly, in condition 2, with $L=0.40$ m, cracks with $n=8$–11 cannot be induced to propagate completely. In condition 3, with $L=0.44$ m, cracks with $n=8$–11 cannot be induced to propagate completely. According to Eq. (10), the calculated values of x are 60, 50, and 44 for the three conditions, respectively. All three conditions have a threshold value for x: when x is approximately 50, the influence of voids is not significant enough to cause complete crack propagation.

From the observation of Fig. 8a, it can be noted that as L increases, n also increases. Additionally, the slope of the L-n curve for all three conditions increases with L, indicating a decreasing influence of empty holes. Examining Fig. 8b, it can be seen that for all three conditions, f decreases with increasing L. As the charge weight increases, the corresponding f for the same spacing L becomes larger. Moreover, when x reaches the threshold, f is consistently below 80% (as indicated by the three points in the box in the lower part of the figure).

Based on the analysis of the numerical simulation data, including the spacing L and charge weight parameters, an empirical formula has been fitted as shown in Fig. 9. The range of x values considered is $0 \le x < 50$, and the coefficient of determination $R^2=0.89$.

In summary, there exists a threshold value for x ($x=50$). When this threshold is reached, the above equation is no longer applicable. At this point, the inducing effect of empty holes on blast-induced fractures becomes insignificant, leading to incomplete crack propagation. Even if crack propagation is achievable, it requires a larger number of empty

Table 3 Model mechanical parameters

Condition 1			Condition 2			Condition 3		
L (m)	n (-)	L_1 (m)	L (m)	n (-)	L_1 (m)	L (m)	n (-)	L_1 (m)
0.12	0	0.12	0.12	0	0.12	0.12	0	0.12
0.16	2	0.15	0.16	0	0.16	0.16	0	0.16
0.20	3	0.18	0.20	1	0.19	0.20	0	0.20
0.24	4	0.22	0.24	3	0.22	0.24	2	0.22
0.28	5	0.25	0.28	4	0.25	0.28	2	0.26
0.32	7	0.28	0.32	4	0.29	0.32	3	0.29
0.36	8–11	No	0.36	7	0.30	0.36	5	0.31
			0.40	8–11	No	0.40	7	0.33
						0.44	8–11	No

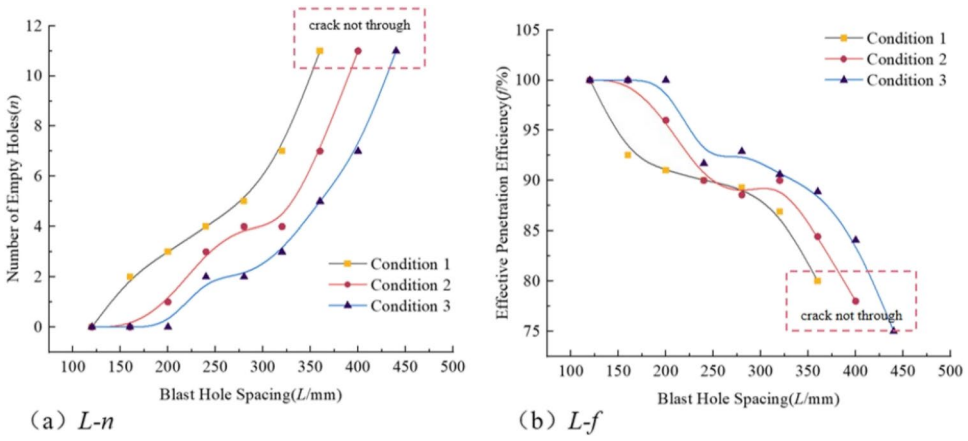

Fig. 8 Three working conditions curve

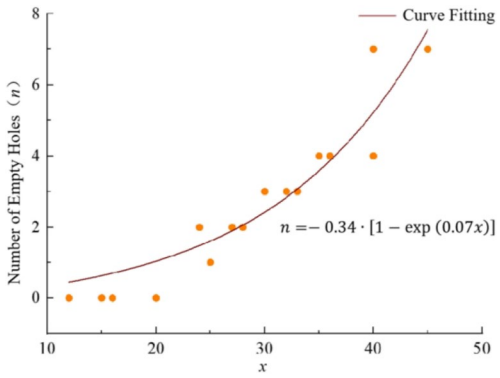

Fig. 9 Empirical formula curve

holes, resulting in a reduced effective propagation distance and diminished cost-effectiveness of borehole excavation. In such cases, it is necessary to increase the explosive equivalent to achieve complete crack propagation. When x is within the threshold range, the above equation can be used to determine the optimal number of voids for inducing crack propagation.

5 Conclusion

In this study, a two-dimensional double-hole blasting numerical model was established using the continuous-discontinuous element method (CDEM). The feasibility of the numerical method was validated by comparing the results with experimental data, showing a high level of agreement between them. By leveraging the central hole effect, multiple working conditions were simulated by varying the charge parameters. Optimal numbers of empty holes for specific blast hole spacing were determined through fitting, leading to the following conclusions:

1. An empirical formula was derived by fitting the numerical simulation results, which was used to determine the optimal number of empty holes for inducing crack propagation. The formula's applicable range is defined as $0 \le x < 50$.
2. When arranging empty holes between blast holes, the following guidelines are followed: For $0 \le x < 20$, 0–1 empty holes are placed. For $20 \le x < 30$, 1–3 empty holes are placed. For $30 \le x < 40$, 3–4 empty holes are placed. For $40 \le x < 50$, 4–7 empty holes are placed. When $x \ge 50$ reaches the threshold, empty hole placement cannot induce crack propagation, and it is necessary to increase the explosive equivalent to achieve crack propagation. During empty hole fabrication, the empty hole diameter is the same as that of the charge hole, and the empty holes are evenly distributed among the charge holes based on the number of empty holes to be placed.

In this study, the influence of multiple empty holes on the propagation of blast-induced cracks was analyzed. By fitting the data, the optimal number of voids required for inducing crack propagation was determined under specific blasthole spacing conditions. These findings provide valuable insights for further investigating the empty hole effect and improving blasting effectiveness. The research outcomes have significant implications for the precise optimization and design of parameters for blasting empty holes.

Funding The authors received financial support from the National Natural Science Foundation of China (NSFC) (52178324).

Declarations

Conflict of Interest The authors declare no competing interests.

References

1. Fourney WL, Holloway DC, Dally JW (1975) Fracture initiation and propagation from a center of dilatation. Int J Fract 11:1011–1029. https://doi.org/10.1007/BF00033847
2. Singh PK, Roy MP, Paswan, Ranjit K (2014) Controlled blasting for long term stability of pit-walls. Int J Rock Mech Min Sci 70:388–399. https://doi.org/10.1016/j.ijrmms.2014.05.006
3. Fourney WL (1993) Mechanisms of rock fragmentation by blasting. Excavation, Support and Monitoring. 39–69. https://doi.org/10.1016/B978-0-08-042067-7.50009-X
4. Hino K (1956) Fragmentation of rock through blasting and shock wave theory of Blasting. In: Paper presented at the The 1st U.S. Symposium on Rock Mechanics (USRMS). USRMS Golden, Colorado
5. Latham JP, Munjiaza A, Lu P (1999) Rock fragmentation by blasting—a literature study of research in the 1980's and 1990's. Fragblast 3:193–212. https://doi.org/10.1080/13855149909408046
6. Clark LD, Jones RJ, Howell RC (1971) Blasting mechanics. Trans Am Instit Min Eng. https://doi.org/10.1007/978-94-011-6501-3_17
7. Zhao JJ, Zhang Y, Ranjith PG (2017) Numerical simulation of blasting-induced fracture expansion in coal masses. Int J Rock Mech Min Sci 100:28–39. https://doi.org/10.1016/j.ijrmms.2017.10.015
8. Hu SB, Wang EY, Kong XG (2015) Damage and deformation control equation for gas-bearing coal and its numerical calculation method. J Nat Gas Sci Eng 25:166–179. https://doi.org/10.1016/j.jngse.2015.04.039
9. Guo DY, Zhao JC, Zhu TG, Zhang C (2020) Crack propagation and coalescence mechanism of double-hole cumulative blasting in coal seam. Chin J Eng 42:1613. https://doi.org/10.13374/j.issn2095-9389.2020.05.19.001
10. Yang RS, Wang YB, Yue ZW, Liu GQ (2013) Dynamic behaviors of crack propagation in directional fracture blasting with two holes. Explos Shock Waves 33:631–637

11. Yang RS, Wang YB, Yang LY (2012) Dynamic caustics experimental study of crack propagation in two borehole cut blasting. J China Univ Min Technol 41:865–872
12. Nakamura Y, Cho SH, Yoneoka M, Yamamoto M, Kaneko K (2004) Model experiments on crack propagation between two charge holes in blasting. Sci Technol Energ Mater 65:34–39. https://api.semanticscholar.org/CorpusID:137511495
13. Cho SH, Nakamura Y, Mohanty B, Yang HS, Kaneko K (2008) Numerical study of fracture plane control in laboratory-scale blasting. Eng Fract Mech 75:3966–3984. https://doi.org/10.1016/J.ENGFRACMECH.2008.02.007
14. Yang RS, Wang YB, Guo DM, Xue HJ (2016) Experimental research of crack propagation in polymethyl methacrylate material containing flaws under explosive stress waves. J Test Eval 44:20140055. https://doi.org/10.1520/JTE20140055
15. Dally JW (1980) An introduction to dynamic photoelasticity. Exp Mech 20:409–416. https://doi.org/10.1007/BF02320881
16. Li SH, Wang JG, Liu BS, Dong D (2007) Analysis of critical excavation depth for a jointed rock slope using a face-to-face discrete element method. Rock Mech Rock Eng 40:331–348. https://doi.org/10.1007/s00603-006-0084-9
17 Wang YN, Zhao MH, Li SH, Wang JG (2015) Stochastic structural model of rock and soil aggregates by continuum-based discrete element method. Sci China: Techn Sci z1:12. https://doi.org/10.1360/04zze13
18. Feng C, Liu XM, Lin QD, Li SH (2022) A simple particle-spring method for capturing the continuous-discontinuous processes of brittle materials. Eng Anal Boundary Elem 139:221–231. https://doi.org/10.1016/j.enganabound.2022.03.015
19. Li SH, Zhao MH, Wang YN, Rao Y (2004) A new numerical method for dem - block and particle model. Int J Rock Mech Min Sci 41:414–418. https://doi.org/10.1016/j.ijrmms.2004.03.076
20. Li SH, Zhao MH, Wang YN, Rao Y (2021) A novel three-dimensional hydraulic fracturing model based on continuum-discontinuum element method. Comput Methods Appl Mech Eng 383:113–887. https://doi.org/10.1016/j.ijrmms.2004.03.076
21. Feng PX, Li YP, Wang XY, Feng C, Zhang YM (2022) Numerical analysis on two-layer bundle-hole cut blasting with continuous-discontinuous elements. Geotech Geol Eng 40:5045–5054. https://doi.org/10.1007/s10706-022-02198-3
22. Wang HZ, Yu AF, Feng C, Ling XD, Chen GX, Gu M, Zhu XQ (2022) An Efficient CDEM-based method to calculate full time-space natural fragment field of shell-bearing explosives. Int J Impact Eng. https://doi.org/10.1016/j.ijimpeng.2021.104099
23. Wang HZ, Yu AF, Feng C, Ling XD, Chen GX, Gu M, Zhu XQ (2019) An efficient CDEM-based method to calculate full-scale fragment field of warhead. Int J Impact Eng 133:103331. https://doi.org/10.1016/j.ijimpeng.2019.103331
24. Ding CX, Yang RS, Zheng CD, Yang LY, He SL, Feng C (2021) Numerical analysis of deep hole multi-stage cut blasting of vertical shaft using a continuum-based discrete element method. Int J Impact Eng 14:1086. https://doi.org/10.1007/s12517-021-07425-4
25. Ding CX, Yang RS, Zheng CD, Yang LY, He SL, Feng C (2021) Hydraulic fracturing characteristics of water resisting rock mass with layered joints based on CDEM. Hazard Control Tunn Undergr Eng 3:9. https://doi.org/10.19952/j.cnki.2096-5052.2021.03.08
26. Zheng BX, Feng C, Song JQ, Guo RK, Li SH (2015) Numerical simulation study on the influence of explosive consumption on the fragmentation of hematite blasting. Blasting 32:8. https://doi.org/10.3963/j.issn.1001-478X.2015.03.011
27. Ding CX, Yang RS, Yang LY (2021) Experimental results of blast-induced cracking fractal characteristics and propagation behavior in deep rock mass. Int J Rock Mech Min Sci 142:104772. https://doi.org/10.1016/j.ijrmms.2021.104772
28. Ding CX, Yang RS, Lei Z, Wang M, Zhao Y, Lin H (2021) Fractal damage and crack propagation in decoupled charge blasting. Soil Dyn Earthq Eng 141:106503. https://doi.org/10.1016/j.soildyn.2020.106503
29. Yang RS, Ding CX, Yang LY (2016) Experimental study on interaction effect of dynamic cracks induced by blast. Blasting 33:2